

# Sparse-View X-Ray CT Reconstruction Using $\ell_1$ Prior with Learned Transform

Xuehang Zheng<sup>†</sup>, Il Yong Chun<sup>†</sup>, *Member, IEEE*, Zhipeng Li,  
Yong Long\*, *Member, IEEE*, and Jeffrey A. Fessler, *Fellow, IEEE*

**Abstract**—A major challenge in X-ray computed tomography (CT) is reducing radiation dose while maintaining high quality of reconstructed images. To reduce the radiation dose, one can reduce the number of projection views (sparse-view CT); however, it becomes difficult to achieve high quality image reconstruction as the number of projection views decreases. Researchers have applied the concept of learning sparse representations from (high-quality) CT image dataset to the sparse-view CT reconstruction. We propose a new statistical CT reconstruction model that combines penalized weighted-least squares (PWLS) and  $\ell_1$  regularization with learned sparsifying transform (PWLS-ST- $\ell_1$ ), and an algorithm for PWLS-ST- $\ell_1$ . Numerical experiments for sparse-view 2D fan-beam CT and 3D axial cone-beam CT show that the  $\ell_1$  regularizer significantly improves the sharpness of edges of reconstructed images compared to the CT reconstruction methods using edge-preserving regularizer and  $\ell_2$  regularization with learned ST.

**Index Terms**—Sparse-view CT, Statistical image reconstruction, Machine learning, Dictionary learning, Transform learning, Sparse representations,  $\ell_1$ -norm regularization.

## I. INTRODUCTION

Radiation dose reduction is a major challenge in X-ray computed tomography (CT). Sparse-view CT reduces dose by acquiring fewer projection views [1], [2]. However, as the number of projection views decreases, it becomes harder to achieve high quality (high resolution, contrast, and signal-to-noise ratio) image reconstruction. Inspired by compressed sensing theories exploiting sparsity of signal [3]–[5], there have been extensive studies for sparse-view CT reconstruction with total variation [6]–[10] or other sparsity promoting regularizers [1], [2].

Learning prior information from big datasets of CT images and exploiting it for solving inverse problems is a recent approach. This idea has been widely applied in image denoising problems and provided promising results [11]–[15]. Recently, patch-based sparse representation learning frameworks [11]–[13] have been successfully applied to improve low-dose CT reconstruction [16]–[19]. The authors in [19] reported that multiple transforms learned via clustering different features can further improve image quality of reconstructions over the low-dose CT reconstruction method using a single sparsifying

transform (ST) in [18]. In [17], it was shown that replacing a  $\ell_2$  dictionary learning regularization with a  $\ell_1$  one improves accuracy of low-dose CT reconstruction.

Researchers have applied (deep) networks to sparse-view and low-dose CT reconstruction problems. Early stage works focused on image denoising [20]–[23]. More recent works combined CT physics-based models and the image mapping networks (or image denoising prior, e.g., sparse coding step in our work—see Section II-C2) [24], [25]. However, it is difficult to mathematically formulate their “full” reconstruction models, and this limits comprehensively understanding/analyzing them.

This work started from a simple observation in our recent study [18]: CT reconstruction with a  $\ell_2$  regularizer using a learned ST has difficulty in reconstructing sharp edges. The question then arises, “Does the learned prior experience model mismatch in testing stage?”. To answer this question, we aim to investigate learned STs for regularization. This paper proposes 1) a new (statistical) CT reconstruction model that combines penalized weighted-least squares (PWLS) and  $\ell_1$  regularization with learned ST (PWLS-ST- $\ell_1$ ) and 2) a corresponding algorithm based on Alternating Direction Method of Multipliers (ADMM) [26]. A similar approach is introduced in [17]; however, there are several notable differences:

- 1) We focus on an analysis (e.g., transform) approach; on the other hand, [17] is based on a synthesis (e.g., dictionary) perspective.
- 2) We pre-learn our signal model and exploit it in CT reconstruction as a prior, whereas [17] adaptively estimates the dictionary in reconstruction stage. Because their dictionary changes during reconstruction, their main concern is not related to the model mismatch.
- 3) We directly attack  $\ell_1$  minimization via ADMM; the algorithm in [17] is based on a reweighted- $\ell_2$  minimization framework.

The remainder of this paper is organized as follows. Section II describes the formulations for pre-learning a square transform, and the formulation and algorithm for PWLS reconstruction using  $\ell_1$ -regularization with learned ST. Section III reports numerical experiments with the XCAT phantom: for sparse-view 2D fan-beam CT and 3D axial cone-beam CT, the proposed PWLS-ST- $\ell_1$  model significantly improves the edge sharpness of reconstructed images compared to a PWLS reconstruction method with an edge-preserving (EP) (hyperbola) regularizer (PWLS-EP) and to  $\ell_2$  regularization with a learned ST (PWLS-ST- $\ell_2$  [18]). Section IV presents our conclusions and mentions future directions.

<sup>†</sup>These two authors contributed equally to this work.

This work is supported in part by UM-SJTU Collaborative Research Program, NSFC (61501292), Shanghai Pujiang Talent Program (15PJ1403900), and NIH Grant U01 EB018753. Asterisk indicates the corresponding author.

Xuehang Zheng, Zhipeng Li and Yong Long are with the University of Michigan - Shanghai Jiao Tong University Joint Institute, Shanghai Jiao Tong University, Shanghai 200240, China (email: {zhxhang, zhipengli, yong.long}@sjtu.edu.cn).

Il Yong Chun and Jeffrey A. Fessler are with the Department of Electrical Engineering and Computer Science, The University of Michigan, Ann Arbor, MI 48019 USA (email: {iyochun, fessler}@umich.edu).

## II. METHODS

The proposed approach has two stages. The first stage is to learn a square ST from good quality CT images used as training data. Then the learned ST is used for regularized reconstruction of lower dose (or sparse view) CT data. This section summarizes the cost functions and algorithms for both stages.

### A. Offline Learning Sparsifying Transform

We pre-learn a ST by solving the following problem [13] (mathematical notations are detailed in Appendix A.):

$$\operatorname{argmin}_{\Psi \in \mathbb{R}^{n \times n}} \min_{\{\mathbf{z}'_j \in \mathbb{R}^n\}} \sum_{j=1}^{J'} \|\Psi \mathbf{x}'_j - \mathbf{z}'_j\|_2^2 + \gamma' \|\mathbf{z}'_j\|_0 + \tau (\xi \|\Psi\|_F^2 - \log |\det \Psi|) \quad (1)$$

where  $\Psi \in \mathbb{R}^{n \times n}$  is a square ST,  $\{\mathbf{x}'_j \in \mathbb{R}^n : j = 1, \dots, J'\}$  is a set of  $J'$  patches extracted from training data,  $\mathbf{z}'_j \in \mathbb{R}^n$  is the sparse code corresponding to the  $j$ th patch  $\mathbf{x}'_j$ ,  $J'$  is the total number of the image patches, and  $\gamma', \tau, \xi \in \mathbb{R}$  are regularization parameters.

### B. CT Reconstruction Model Using $\ell_1$ -Regularization with Learned Sparsifying Transform: PWLS-ST- $\ell_1$

To reconstruct a linear attenuation coefficient image  $\mathbf{x} \in \mathbb{R}^N$  from post-log measurement  $\mathbf{y} \in \mathbb{R}^m$  [2], we solve the following non-convex optimization problem using PWLS and the ST  $\Psi$  learned via (1):

$$\operatorname{argmin}_{\mathbf{x} \in \mathbb{R}^N} \min_{\mathbf{z} \in \mathbb{R}^{nJ}} \frac{1}{2} \|\mathbf{y} - \mathbf{A}\mathbf{x}\|_{\mathbf{W}}^2 + \lambda \|\tilde{\Psi}\mathbf{x} - \mathbf{z}\|_1 + \gamma \|\mathbf{z}\|_0, \quad (2)$$

where

$$\tilde{\Psi} = \begin{bmatrix} \Psi \mathbf{P}_1 \\ \vdots \\ \Psi \mathbf{P}_J \end{bmatrix} \quad \text{and} \quad \mathbf{z} = \begin{bmatrix} \mathbf{z}_1 \\ \vdots \\ \mathbf{z}_J \end{bmatrix}.$$

Here,  $\mathbf{A} \in \mathbb{R}^{m \times N}$  is a CT scan system matrix,  $\mathbf{W} \in \mathbb{R}^{m \times m}$  is a diagonal weighting matrix with elements  $\{W_{l,l} = \rho_l^2 / (\rho_l + \sigma^2) : l = 1, \dots, m\}$  based on a Poisson-Gaussian model for the pre-log measurements  $\boldsymbol{\rho} \in \mathbb{R}^m$  with electronic readout noise variance  $\sigma^2$  [2], [27],  $\mathbf{P}_j \in \mathbb{R}^{n \times N}$  is a patch-extraction operator for the  $j$ th patch,  $\mathbf{z}_j \in \mathbb{R}^n$  is unknown sparse code for the  $j$ th patch,  $J$  is the number of extracted patches, and  $\lambda, \gamma > 0$  are regularization parameters.

The term  $\|\tilde{\Psi}\mathbf{x} - \mathbf{z}\|_1$  denotes an  $\ell_1$ -based sparsification error [3]–[5]. We expect  $\ell_1$  to be more robust to sparsity model mismatch than the  $\ell_2$ -based sparsification error used in [18]. In particular, the proposed  $\ell_1$ -based sparsification error term,  $\|\tilde{\Psi}\mathbf{x} - \mathbf{z}\|_1$ , preserves edge sharpness better than  $\|\tilde{\Psi}\mathbf{x} - \mathbf{z}\|_2^2$  in [18] (see Fig. 3–4 and Table I).

### C. Proposed Algorithm for PWLS-ST- $\ell_1$

To solve (2), our proposed algorithm alternates between updating the image  $\mathbf{x}$  (*image update step*) and the sparse codes  $\mathbf{z}$  (*sparse coding step*). For the image update, we apply ADMM [2], [9], [26]—simply put, it introduces an

auxiliary variable to separate the effects of a certain variable or combinations of variables (called variable splitting in [9], [28]). For efficient sparse coding, we apply an analytical solution for  $\mathbf{z}$ . The following subsections provide algorithmic details for solving (2), summarize them in Algorithm 1, and provide underlying intuitions.

1) *Image Update - ADMM*: Using the current sparse code estimates  $\mathbf{z}$ , we update the image  $\mathbf{x}$  by augmenting (2) with auxiliary variables [9]:

$$\min_{\substack{\mathbf{x}, \mathbf{d}_a \in \mathbb{R}^m, \\ \mathbf{d}_\psi \in \mathbb{R}^{nJ}}} \frac{1}{2} \|\mathbf{y} - \mathbf{d}_a\|_{\mathbf{W}}^2 + \lambda \|\mathbf{d}_\psi\|_1$$

$$\text{subject to} \quad \begin{bmatrix} \mathbf{d}_a \\ \mathbf{d}_\psi \end{bmatrix} = \begin{bmatrix} \mathbf{A} \\ \tilde{\Psi} \end{bmatrix} \mathbf{x} - \begin{bmatrix} \mathbf{0} \\ \mathbf{z} \end{bmatrix}.$$

The corresponding augmented Lagrangian has the form

$$\frac{1}{2} \|\mathbf{y} - \mathbf{d}_a\|_{\mathbf{W}}^2 + \lambda \|\mathbf{d}_\psi\|_1 + \frac{\mu}{2} \|\mathbf{d}_a - \mathbf{A}\mathbf{x} - \mathbf{b}_a\|_2^2 + \frac{\mu\nu}{2} \|\mathbf{d}_\psi - (\tilde{\Psi}\mathbf{x} - \mathbf{z}) - \mathbf{b}_\psi\|_2^2.$$

We descend/ascend this augmented Lagrangian using the following iterative updates of the primal, auxiliary, dual variables— $\mathbf{x}$ ,  $\{\mathbf{d}_a, \mathbf{d}_\psi\}$ , and  $\{\mathbf{b}_a, \mathbf{b}_\psi\}$ , respectively:

$$\mathbf{x}^{(i+1)} = \left( \mathbf{A}^T \mathbf{A} + \nu \sum_{j=1}^J \mathbf{P}_j^T \Psi^T \Psi \mathbf{P}_j \right)^{-1} \left( \mathbf{A}^T (\mathbf{d}_a^{(i)} - \mathbf{b}_a^{(i)}) + \nu \tilde{\Psi}^T (\mathbf{d}_\psi^{(i)} - \mathbf{b}_\psi^{(i)} + \mathbf{z}) \right); \quad (3)$$

$$\mathbf{d}_a^{(i+1)} = (\mathbf{W} + \mu \mathbf{I}_m)^{-1} (\mathbf{W}\mathbf{y} + \mu (\mathbf{A}\mathbf{x}^{(i+1)} + \mathbf{b}_a^{(i)})); \quad (4)$$

$$d_{\psi,u}^{(i+1)} = \operatorname{softshrink} \left( \left( \tilde{\Psi}\mathbf{x}^{(i+1)} - \mathbf{z} + \mathbf{b}_\psi^{(i)} \right)_u, \frac{\lambda}{\mu\nu} \right),$$

$$u = 1, \dots, nJ;$$

$$\mathbf{b}_a^{(i+1)} = \mathbf{b}_a^{(i)} - \left( \mathbf{d}_a^{(i+1)} - \mathbf{A}\mathbf{x}^{(i+1)} \right);$$

$$\mathbf{b}_\psi^{(i+1)} = \mathbf{b}_\psi^{(i)} - \left( \mathbf{d}_\psi^{(i+1)} - (\tilde{\Psi}\mathbf{x}^{(i+1)} - \mathbf{z}) \right),$$

where the soft-shrinkage operator is defined by  $\operatorname{softshrink}(\alpha, \beta) := \operatorname{sign}(\alpha) \max(|\alpha| - \beta, 0)$ . To approximately solve (3), we use the preconditioned conjugate gradient (PCG) method with a preconditioner  $\mathbf{M}$  for  $\mathbf{A}^T \mathbf{A} + \nu \sum_{j=1}^J \mathbf{P}_j^T \Psi^T \Psi \mathbf{P}_j$ . PCG( $\mathbf{M}$ ) denotes PCG method using a preconditioner  $\mathbf{M}$ ; see Algorithm 1.

2) *Sparse Coding*: Given the current estimates of the image  $\mathbf{x}$ , we update the sparse codes  $\mathbf{z}$  by solving the following optimization problem:

$$\min_{\mathbf{z} \in \mathbb{R}^{nJ}} \lambda \|\tilde{\Psi}\mathbf{x} - \mathbf{z}\|_1 + \gamma \|\mathbf{z}\|_0. \quad (5)$$

Proposition 2.1 provides an optimal solution of (5) as an element-wise operator:

$$z_j^* = \operatorname{hardshrink} \left( \left( \tilde{\Psi}\mathbf{x} \right)_j, \frac{\gamma}{\lambda} \right), \quad j = 1, \dots, nJ, \quad (6)$$

---

**Algorithm 1** PWLS-ST- $\ell_1$  CT Reconstruction
 

---

**Require:**  $\mathbf{y}$ ,  $\mathbf{x}^{(1)}$ ,  $\mathbf{z}^{(1)}$ ,  $\Psi$  learned from (1),  $\mathbf{M}$ ,  $\mathbf{W}$ ,  $\lambda, \gamma, \mu, \nu \geq 0$ ,  $i = 1$

**while** a stopping criterion is not satisfied **do**

**for**  $i' = 1, \dots, \text{Iter}_{\text{ADMM}}$  **do**

    Obtain  $\tilde{\mathbf{x}}^{(i'+1)}$  by solving (3) with PCG( $\mathbf{M}$ )

$$\mathbf{d}_a^{(i'+1)} = (\mathbf{W} + \mu \mathbf{I}_m)^{-1} (\mathbf{W} \mathbf{y} + \mu (\mathbf{A} \tilde{\mathbf{x}}^{(i'+1)} + \mathbf{b}_a^{(i')}))$$

$$\mathbf{d}_{\psi, j}^{(i'+1)} = \text{softshrink} \left( \left( \tilde{\Psi} \tilde{\mathbf{x}}^{(i'+1)} - \mathbf{z}^{(i)} + \mathbf{b}_{\psi}^{(i')} \right)_j, \frac{\lambda}{\mu \nu} \right),$$

$$\mathbf{b}_a^{(i'+1)} = \mathbf{b}_a^{(i')} - \left( \mathbf{d}_a^{(i'+1)} - \mathbf{A} \tilde{\mathbf{x}}^{(i'+1)} \right)$$

$$\mathbf{b}_{\psi}^{(i'+1)} = \mathbf{b}_{\psi}^{(i')} - \left( \mathbf{d}_{\psi}^{(i'+1)} - \left( \tilde{\Psi} \tilde{\mathbf{x}}^{(i'+1)} - \mathbf{z}^{(i)} \right) \right),$$

**end for**

$$\mathbf{x}^{(i+1)} = \tilde{\mathbf{x}}^{(\text{Iter}_{\text{ADMM}}+1)}$$

$$\mathbf{z}_j^{(i+1)} = \text{hardshrink} \left( \left( \tilde{\Psi} \mathbf{x}^{(i+1)} \right)_j, \frac{\gamma}{\lambda} \right), j = 1, \dots, nJ$$

$i = i + 1$

**end while**

---

where the hard-shrinkage operator is defined by

$$\text{hardshrink}(\alpha, \beta) := \begin{cases} \alpha, & |\alpha| \geq \beta, \\ 0, & |\alpha| < \beta. \end{cases} \quad (7)$$

According to Proposition 2.1 below, (6) is the optimal estimator of the vector  $\tilde{\Psi} \mathbf{x}$  in (5) among all sparse vectors having cardinality no greater than that of  $\mathbf{z}^*$ .

**Proposition 2.1.** *For any given vector  $\mathbf{u}$ , the minimization problem*

$$\min_{\mathbf{z}} \|\mathbf{u} - \mathbf{z}\|_1 + \theta \|\mathbf{z}\|_0, \quad \theta > 0, \quad (8)$$

*has an optimal solution*

$$\mathbf{z}_j^* = \text{hardshrink}(u_j, \theta), \quad \forall j,$$

*where  $\text{hardshrink}(\alpha, \beta)$  is given as (7). In addition, for any  $\mathbf{z}$  satisfying  $\|\mathbf{z}\|_0 \leq \|\mathbf{z}^*\|_0$ ,*

$$\|\mathbf{u} - \mathbf{z}\|_1 \geq \|\mathbf{u} - \mathbf{z}^*\|_1.$$

*Proof.* See Appendix B.

One should set  $\gamma$  properly based on the (estimated) values of  $\tilde{\Psi} \mathbf{x}$ . If  $\gamma$  is too large compared to these values, the operator in (6) may remove the sparse code coefficients corresponding to some edges in low-contrast regions (e.g., soft tissues); if  $\gamma$  is too small, then (6) will not properly remove noise (or unwanted artifacts).

3) *Preconditioner Design for Solving (3) via PCG:* For a 2D fan-beam CT problem, a circulant preconditioner is well suited because 1) it is effective for the “nearly” shift-invariant matrix  $\mathbf{A}^T \mathbf{A}$  [2], [9] and 2)  $\sum_{j=1}^J \mathbf{P}_j^T \Psi^T \Psi \mathbf{P}_j$  is a block circulant circulant block (BCCB) matrix when we use the overlapping “stride” 1 and the “wrap around” image patch assumption [29, Prop. 3.3]. For an orthogonal transform  $\Psi$ ,  $\sum_{j=1}^J \mathbf{P}_j^T \Psi^T \Psi \mathbf{P}_j$  is approximately  $(n/\nu) \mathbf{I}_N$  ( $\nu$  denotes the stride parameter). Therefore, a circulant preconditioner is a reasonable choice to approximate  $\mathbf{A}^T \mathbf{A} + \nu \sum_{j=1}^J \mathbf{P}_j^T \Psi^T \Psi \mathbf{P}_j$  in 2D fan-beam CT.

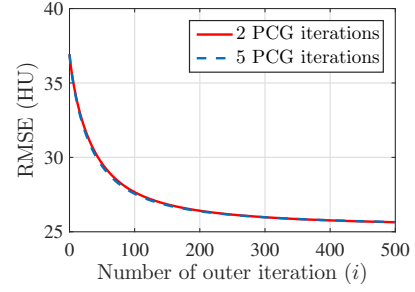


Fig. 1. Comparison of the RMSE convergence behavior for PWLS-ST- $\ell_1$  with 2 and 5 PCG iterations in 3D cone-beam CT reconstruction (123 views;  $\lambda = 8 \times 10^6$ ,  $\gamma/\lambda = 18$ ,  $\kappa_{\text{des}, \nu} = 10$ ,  $\kappa_{\text{des}, \mu} = 40$ ). Although a circulant preconditioner is known to be less accurate to approximate  $\mathbf{A}^T \mathbf{A}$  in (3) for the 3D CT problem, Algorithm 1 using it with 2 PCG iterations gives a similar convergence rate compared to that with 5 PCG iterations.

For a 3D cone-beam CT problem, circulant preconditioning is less accurate because the matrix  $\mathbf{A}^T \mathbf{A}$  is inherently shift-variant due to the system geometry and/or spatial variations in detector response [30]. Despite this fact, we select a circulant preconditioner to approximate  $\mathbf{A}^T \mathbf{A} + \nu \sum_{j=1}^J \mathbf{P}_j^T \Psi^T \Psi \mathbf{P}_j$ , and solve (3) in 3D CT reconstruction with an expected cost of more PCG iterations. The reason is three fold. First, a circulant preconditioner is still one of the classical options to approximate a shift-variant matrix (e.g.,  $\mathbf{A}^T \mathbf{A}$ ) and accelerate CG (see, for example, [30], [31]). Second, effective learned transforms are generally close to orthogonal (the same applies to the 2D case), and a scaled identity preconditioner can approximate the term  $\sum_{j=1}^J \mathbf{P}_j^T \Psi^T \Psi \mathbf{P}_j$ . A few PCG iterations in Algorithm 1 can provide fast convergence: 1) Fig. 1 shows that 2 and 5 PCG iterations give very similar convergence rates; 2) in the 3D CT reconstruction, the convergence rates of Algorithm 1 are comparable to those provided in 2D CT reconstruction—see Fig. 2. More sophisticated preconditioners might provide faster convergence [32], [33].

4) *Parameter selection based on condition numbers:* In practice, ADMM can require difficult parameter tuning processes for fast and stable convergence. We moderate this problem by selecting ADMM parameters (e.g.,  $\nu, \mu$ ) based on (approximated) condition numbers [9]. Observe that, for two square Hermitian matrices  $\mathbf{A} \succeq 0$  and  $\mathbf{B} \succ 0$ ,

$$\kappa(\mathbf{A} + \mathbf{B}) := \frac{\sigma_{\max}(\mathbf{A} + \mathbf{B})}{\sigma_{\min}(\mathbf{A} + \mathbf{B})} \leq \frac{\sigma_{\max}(\mathbf{A}) + \sigma_{\max}(\mathbf{B})}{\sigma_{\min}(\mathbf{A}) + \sigma_{\min}(\mathbf{B})}, \quad (9)$$

by Weyl’s inequality, where the notations  $\kappa(\cdot)$ ,  $\sigma_{\max}(\cdot)$ , and  $\sigma_{\min}(\cdot)$  denote the condition number, the largest eigenvalue, and the smallest eigenvalue of a matrix, respectively. Applying the bound (9) to (3), we select  $\nu$  by

$$\nu = \frac{\sigma_{\max}(\Lambda_{\mathbf{A}}) - \kappa_{\text{des}, \nu} \cdot \sigma_{\min}(\Lambda_{\mathbf{A}})}{\kappa_{\text{des}, \nu} \cdot \sigma_{\min}(\Lambda_{\tilde{\Psi}}) - \sigma_{\max}(\Lambda_{\tilde{\Psi}})} \quad (10)$$

where  $\kappa_{\text{des}, \nu}$  denotes the desired “upper bounded” condition number of  $\mathbf{A}^T \mathbf{A} + \nu \sum_{j=1}^J \mathbf{P}_j^T \Psi^T \Psi \mathbf{P}_j$ , and  $\Lambda_{\mathbf{A}}$  and  $\Lambda_{\tilde{\Psi}}$  are approximated eigenvalue matrices of  $\mathbf{A}^T \mathbf{A}$  and  $\tilde{\Psi}^T \tilde{\Psi}$  by using their circulant preconditioners in Section II-C1, respectively. (The eigenvalue approximation for  $\mathbf{A}^T \mathbf{A}$  and  $\tilde{\Psi}^T \tilde{\Psi}$  can be improved by the power iteration used in [9], with a cost of higher computational complexity.) Note that

equality holds in (9) when either  $\mathbf{A}$  or  $\mathbf{B}$  is a scaled identity matrix. In other words,  $\kappa_{\text{des},\nu}$  becomes close to the condition number of approximated  $\mathbf{A}^T \mathbf{A} + \nu \sum_{j=1}^J \mathbf{P}_j^T \Psi^T \Psi \mathbf{P}_j$ , when the learned ST  $\Psi$  is close to orthogonal. We select  $\mu$  for (4) by

$$\mu = \frac{\sigma_{\max}(\mathbf{W}) - \kappa_{\text{des},\mu} \cdot \sigma_{\min}(\mathbf{W})}{\kappa_{\text{des},\mu} - 1}, \quad (11)$$

where  $\kappa_{\text{des},\mu}$  denotes the desired condition number of  $\mathbf{W} + \mu \mathbf{I}_m$  in (4). We empirically found that  $\kappa_{\text{des},\nu}, \kappa_{\text{des},\mu} \in [10, 50]$  are reasonable values for fast and stable convergence.

5) *Intuitions behind Algorithm 1*: The underlying idea of the image reconstruction model (2) is that the signal is very sparse in the learned transform ( $\Psi$ )-domain, i.e.,  $\tilde{\Psi} \mathbf{x}$  has a few large coefficients, usually corresponding to local high-frequency features (e.g., edges). Thresholding in the sparse coding step, i.e., (6), removes the noise in the other components while preserving the large signal coefficients. Substituting the denoised sparse codes  $\mathbf{z}$  to the image updating optimization, we estimate an image  $\mathbf{x}$  close to the denoised sparse codes in  $\Psi$ -domain, while being robust to the model mismatch in  $\tilde{\Psi} \mathbf{x}$  and  $\mathbf{z}$ . Repeating these processes, we expect to obtain reconstructed images with higher accuracy.

### III. EXPERIMENTAL RESULTS AND DISCUSSION

#### A. Experimental Setup

We evaluated the proposed PWLS-ST- $\ell_1$  method for sparse-view CT reconstruction with 2D fan-beam and 3D axial cone-beam scans of the XCAT phantom [34], and compared the quality of images reconstructed by:

- *FBP*: conventional filtered back-projection method using a Hanning window (for 3D experiments, the Feldkamp-Davis-Kress method [35] is used).
- *PWLS-EP*: PWLS reconstruction method using an edge-preserving regularizer  $\sum_{j=1}^N \sum_{k \in N_j} \ell_j \ell_k \varphi(x_j - x_k)$ , where  $N_j$  is the size of the neighborhood,  $\ell_j$  and  $\ell_k$  are regularization parameters that encourage uniform noise [36], and  $\varphi(t) := \delta^2 \left( \sqrt{1 + |t/\delta|^2} - 1 \right)$  for 2D,  $\varphi(t) := \delta^2 (|t/\delta| - \log(1 + |t/\delta|))$  for 3D ( $\delta = 10$  in Hounsfield units<sup>1</sup>, HU). We adopted the relaxed linearized augmented Lagrangian method with ordered-subsets (relaxed OS-LALM) proposed in [37] to accelerate the reconstruction.
- *PWLS-ST- $\ell_2$* : PWLS reconstruction method using  $\ell_2$  regularization with a learned ST [18], [19]. For fair comparison, we performed the image update of the algorithm proposed for PWLS-ST- $\ell_2$  without the non-nonnegativity constraint.

We quantitatively evaluated the reconstruction quality by RMSE (in HU) in a region of interest (ROI). The RMSE is defined by  $\text{RMSE} := (\sum_{j=1}^{N_{\text{ROI}}} (\hat{x}_j - x_j^{\text{true}})^2 / N_{\text{ROI}})^{1/2}$ , where  $\hat{\mathbf{x}}$  is the reconstructed image (after clipping non-negative values),  $\mathbf{x}^{\text{true}}$  is the ground truth image, and  $N_{\text{ROI}}$  is the number of pixels in a ROI.

<sup>1</sup>Modied Hounsfield units, where air is 0 HU and water is 1000 HU.

1) *2D Fan-beam - Imaging*: To avoid an inverse crime, our 2D imaging simulation used a  $840 \times 840$  slice (air cropped,  $\Delta_x = \Delta_y = 0.4883$  mm) of the XCAT phantom, which is different from the training slices. We simulated sinograms of size 888 (detectors or rays)  $\times$  {246, 123} (regularly spaced projection views or angles; 984 is the number of full views) with GE LightSpeed fan-beam geometry corresponding to a monoenergetic source with  $\rho_0 = 10^5$  incident photons per ray and no background events, and electronic noise variance  $\sigma^2 = 5^2$ . We reconstructed a  $420 \times 420$  image with a coarser grid, where  $\Delta_x = \Delta_y = 0.9766$  mm. The ROI for the 2D case was a circular (around center) region including all the phantom tissues.

2) *2D Fan-beam - Image Reconstruction*: Before executing reconstructions, we pre-learned square STs from  $8 \times 8$  image patches extracted from five different slices of the XCAT phantom (with  $1 \times 1$  overlapping stride). To learn well-conditioned transforms, we chose a large enough  $\tau$ , e.g.,  $\tau = 5.85 \times 10^{14}$ . We chose  $\gamma' = 110$  and  $\xi = 1$ . Initialized with the 2D discrete cosine transform (DCT), we ran 1000 iterations of the alternating minimization algorithm proposed in [13] to ensure learned transforms are well converged.

We initialized the PWLS-EP method with FBP reconstructions, and ran the relaxed OS-LALM [37] for 100 iterations with 12 ordered subsets. We chose the regularization parameter (balancing the data fitting term and the regularizer) as  $2^{15.5}$  and  $2^{15.0}$  for 246 and 123 views, respectively. For both PWLS-ST- $\ell_1$  and PWLS-ST- $\ell_2$  methods, we used a patch size  $8 \times 8$  with a  $1 \times 1$  overlapping stride. We used converged PWLS-EP reconstructions for initialization and set a stopping criterion as meeting the maximum number of iterations, e.g.,  $\text{Iter} = 1000$ . For the image update, we set  $\text{Iter}_{\text{ADMM}} = 2$  (2 PCG iterations [9]) for PWLS-ST- $\ell_1$ ; and set 12 relaxed OS-LALM iterations without ordered subsets for PWLS-ST- $\ell_2$ . For PWLS-ST- $\ell_1$ , we tuned  $\nu, \mu$  using the condition number based selection schemes, i.e.,  $\kappa_{\text{des},\nu}$  in (10) and  $\kappa_{\text{des},\mu}$  in (11). We finely tuned the parameters  $\lambda, \gamma$  to achieve good image quality. For PWLS-ST- $\ell_1$ , we chose  $\{\lambda, \gamma/\lambda, \kappa_{\text{des},\nu}, \kappa_{\text{des},\mu}\}$  as follows:  $\{1.3 \times 10^6, 80, 30, 30\}$  for 246 views;  $\{9 \times 10^5, 80, 30, 30\}$  for 123 views. For PWLS-ST- $\ell_2$  [18], we chose  $\{\lambda, \gamma\}$  as follows:  $\{3 \times 10^5, 20\}$  for 246 views;  $\{1.6 \times 10^5, 20\}$  for 123 views. Note that  $\lambda$  and  $\gamma$  are in HU.

3) *3D Cone-beam - Imaging*: In the 3D CT experiments, we simulated an axial cone-beam CT scan using an  $840 \times 840 \times 96$  XCAT phantom (air cropped,  $\Delta_x = \Delta_y = 0.4883$  mm and  $\Delta_z = 0.625$  mm). We generated sinograms of size 888 (detectors or rays)  $\times$  64 (rows)  $\times$  {246, 123} (984 is the number of full views) using GE LightSpeed cone-beam geometry corresponding to a monoenergetic source with  $\rho_0 = 10^5$  incident photons per ray and no scatter, and  $\sigma^2 = 5^2$ . We reconstructed a  $420 \times 420 \times 96$  volume with a coarser grid, where  $\Delta_x = \Delta_y = 0.9766$  mm and  $\Delta_z = 0.625$  mm. We defined a cylinder ROI for the 3D case, which consists of the central 64 of 96 axial slices and a circular (around center) region in each slice.

4) *3D Cone-beam - Image Reconstruction*: Similar to the 2D experiments, we pre-learned square STs using  $8 \times 8 \times 8$  patches (with an overlapping stride  $2 \times 2 \times 2$ ) extracted from

TABLE I  
RMSE (HU) OF DIFFERENT 2D AND 3D X-RAY CT RECONSTRUCTIONS  
WITH DIFFERENT NUMBER OF PROJECTION VIEWS ( $\rho_0 = 10^5$ )

	Views	FBP	PWLS-EP	PWLS-ST- $\ell_2$	PWLS-ST- $\ell_1$
2D <sup>a</sup>	246	60.5	30.7	26.9	<b>21.5</b>
	123	82.7	35.0	30.9	<b>25.8</b>
3D <sup>b</sup>	246	58.0	29.3	27.2	<b>22.2</b>
	123	80.2	36.9	30.2	<b>25.6</b>

<sup>a</sup>For the 2D CT experiments, fan-beam geometry was used.

<sup>b</sup>For the 3D CT experiments, axial cone-beam geometry was used.

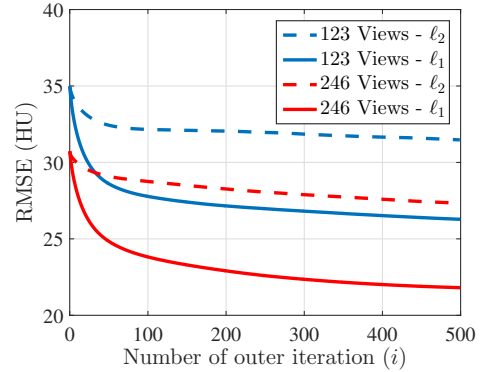
a  $420 \times 420 \times 54$  XCAT phantom, which is different from the phantom used for testing. Initialized with the 3D DCT, we ran the transform learning algorithm [13] for 1000 iterations with  $\tau = 5.63 \times 10^{15}$ ,  $\gamma' = 100$  and  $\xi = 1$ .

For the PWLS-EP method, initialized with FBP reconstructions, we ran the relaxed OS-LALM for 100 iterations with 12 subsets and regularization parameter as  $2^{14}$ , for both 246 and 123 views. For both PWLS-ST- $\ell_1$  and PWLS-ST- $\ell_2$  methods, we chose an  $8 \times 8 \times 8$  patch size with a patch stride  $3 \times 3 \times 3$ . Initialized with converged PWLS-EP reconstructions, we chose a maximum number of iterations  $\text{Iter} = 500$  as the stopping criterion. For the image update, we set  $\text{Iter}_{\text{ADMM}}$  as 2 (we empirically found that 2 PCG iterations provide reasonable convergence behavior, see Fig. 1) for PWLS-ST- $\ell_1$ , and set 2 relaxed OS-LALM iterations with 4 ordered subsets for PWLS-ST- $\ell_2$  [19]. For PWLS-ST- $\ell_1$ , we chose  $\{\lambda, \gamma/\lambda, \kappa_{\text{des},\nu}, \kappa_{\text{des},\mu}\}$  as follows:  $\{1 \times 10^7, 15, 10, 50\}$  for 246 views;  $\{8 \times 10^6, 15, 10, 40\}$  for 123 views. For PWLS-ST- $\ell_2$ , we chose  $\{\lambda, \gamma\}$  as follows:  $\{1 \times 10^6, 18\}$  for 246 views;  $\{8 \times 10^5, 18\}$  for 123 views.

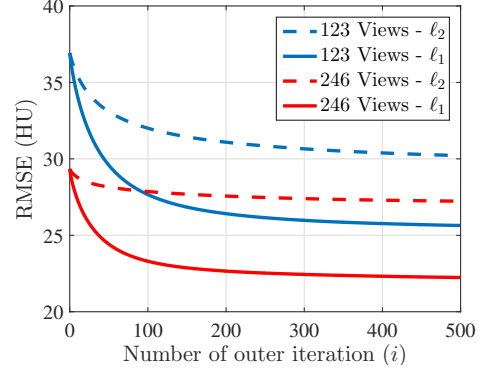
## B. Results and Discussion

1) *Reconstruction Quality*: Table I shows that, for both 2D and 3D sparse-view CT reconstructions, the proposed PWLS-ST- $\ell_1$  model outperforms PWLS-EP and PWLS-ST- $\ell_2$  in terms of RMSE. In particular, PWLS-ST- $\ell_1$  resolves the blurry edge problem in PWLS-ST- $\ell_2$  (see Fig. 3 and Fig. 4). The edge-preserving benefit of PWLS-ST- $\ell_1$  over PWLS-ST- $\ell_2$  can be explained when there exist some outliers for some  $\mathbf{z}^{(i+1)}$ :  $\|\tilde{\Psi}\mathbf{x} - \mathbf{z}^{(i+1)}\|_1$  in (2) gives equal emphasis to all sparse code coefficients—e.g., the components corresponding to edges from low-contrast (e.g., soft tissue) to high-contrast (e.g., bone) regions—in estimating  $\mathbf{x}$ ; however, PWLS-ST- $\ell_2$  adjusts  $\mathbf{x}$  to mainly minimize the outliers, i.e., it may not pay enough attention to reconstruct edges between soft tissues. The proposed PWLS-ST- $\ell_1$  model can accomplish the both benefits of edge-preserving (achieved by PWLS-EP) and image denoising (achieved by PWLS-ST- $\ell_2$ ).

2) *Algorithm Convergence Rate*: Our main concern in convergence rates of Algorithm 1 lies with an inaccurate preconditioner (e.g., circulant one) particularly for the 3D sparse-view CT reconstructions. To see the effects of using a loose preconditioner in Algorithm 1, we compared the convergence rates of the 3D case with those of 2D (Fig. 2(a) and Fig. 2(b)). In the first 100 iterations, Algorithm 1 converges



(a) 2D fan-beam CT experiments



(b) 3D axial cone-beam CT experiments

Fig. 2. RMSE convergence behavior for PWLS-ST- $\ell_1$  and PWLS-ST- $\ell_2$  in different CT geometries and projection views (123 and 246 projection views, and  $\rho_0 = 10^5$ ).

faster in 2D experiments than 3D experiments. However, after 100 iterations, the convergence rates of Algorithm 1 are similar in both 2D and 3D reconstructions. In addition, more PCG (with a circulant preconditioner) iterations does not significantly accelerate Algorithm 1 (see Fig 1). These empirically observations imply that, in the 3D sparse-view CT reconstructions, Algorithm 1 using a circulant preconditioner (2 PCG iterations) is a reasonable choice.

## IV. CONCLUSION

The proposed PWLS-ST- $\ell_1$  model achieves more accurate sparse-view CT reconstruction compared to PWLS-EP and PWLS-ST- $\ell_2$ ; in particular, it leads to sharper edge reconstruction compared to PWLS-ST- $\ell_2$ . This suggests that some model mismatch exists between the training model (1) and the prior term in the PWLS-ST- $\ell_2$  reconstruction, and  $\ell_1$  regularization used in PWLS-ST- $\ell_1$  can moderate this mismatch. Future work will explore PWLS-ST- $\ell_1$  with the technique of controlling local spatial resolution or noise in the reconstructed images [36], [38] to further reduce blur, particularly around the center of reconstructed image (see our results in [39, Appx.] and [19]). On the algorithmic side, we plan to apply *block proximal gradient method using majorizer* [14] to solve nonconvex problem (2) faster and stably, and design a more accurate preconditioner that allows the parameter selection scheme in Section II-C4.

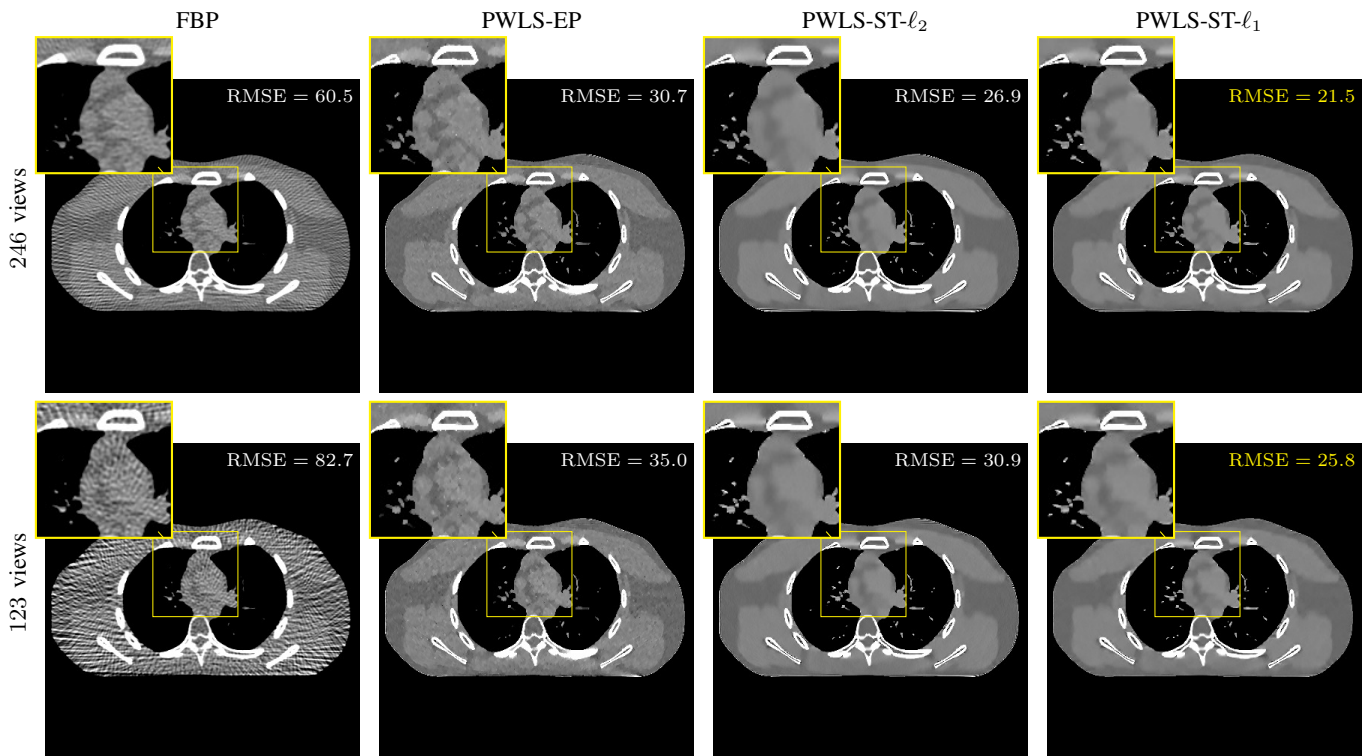


Fig. 3. Comparison of 2D reconstructed images from different X-ray CT reconstruction models with different number of views (2D fan-beam CT geometry and  $\rho_0 = 10^5$ ; display window is [800, 1200] HU; see the ground truth image in Fig. 5). The proposed PWLS-ST- $\ell_1$  consistently improves the sharpness of the reconstructed images over PWLS-ST- $\ell_2$ .



Fig. 4. Comparison of 3D reconstructed images from different X-ray CT reconstruction models with different number of views (axial 3D cone-beam geometry and  $\rho_0 = 10^5$ ; display window is [800, 1200] HU; displayed for the central axial, sagittal, and coronal planes; see the ground truth image in Fig. 5). The proposed PWLS-ST- $\ell_1$  consistently improves the sharpness of the reconstructed images over PWLS-ST- $\ell_2$ .

APPENDIX A  
NOTATION

Bold capital letters represent matrices, and bold lowercase letters are used for vectors (all vectors are column vectors). Italic type is used for all letters representing variables, parameters, and elements of matrices and vectors. We use  $\|\cdot\|_p$  to denote the  $\ell^p$ -norm and write  $\langle \cdot, \cdot \rangle$  for the standard inner product on  $\mathbb{C}^N$ . The weighted  $\ell^2$ -norm with a Hermitian positive definite matrix  $\mathbf{A}$  is denoted by  $\|\cdot\|_{\mathbf{A}} = \|\mathbf{A}^{1/2}(\cdot)\|_2$ .  $\|\cdot\|_0$  denotes the  $\ell^0$ -norm, i.e., the number of nonzeros of a vector. The Frobenius norm of a matrix  $\mathbf{A}$  is denoted by  $\|\mathbf{A}\|_F$ .  $(\cdot)^T$ ,  $(\cdot)^H$  indicate the transpose and complex conjugate transpose (Hermitian transpose), respectively.  $\text{sign}(\cdot)$  and  $\det(\cdot)$  denote the sign function and determinant of a matrix, respectively. For self-adjoint matrices  $\mathbf{A}, \mathbf{B} \in \mathbb{C}^{N \times N}$ , the notation  $\mathbf{B} \preceq \mathbf{A}$  denotes that  $\mathbf{A} - \mathbf{B}$  is a positive semi-definite matrix.

APPENDIX B  
PROOFS OF PROPOSITION 2.1

Define  $g(\alpha) := 0$  if  $\alpha = 0$  and  $g(\alpha) := 1$  otherwise. Since the objective function in (8) equals  $\sum_j |u_j - z_j| + \theta g(z_j)$ , we rewrite (8) as a easily separable minimization problem:

$$\sum_j \min_{z_j} |u_j - z_j| + \theta g(z_j).$$

Considering the separability of (8) and the definition of  $g(\alpha)$ , we have

$$f(z_j) = |u_j - z_j| + \theta g(z_j) = \begin{cases} |u_j|, & z_j = 0, \\ |u_j - z_j| + \theta, & z_j \neq 0. \end{cases} \quad (12)$$

First observe that, if the optimal  $z_j^* = 0$ , then the corresponding optimal objective value is  $f(z_j^*) = |u_j|$ . If  $z_j^* \neq 0$ , then the optimal  $z_j^*$  must be  $u_j$  to minimize the  $|u_j - z_j|$  term in (12); this gives  $f(z_j^*) = \theta$ . Combining these, we have

$$f(z_j^*) = \begin{cases} \theta, & |u_j| \geq \theta, \\ |u_j|, & |u_j| < \theta, \end{cases}$$

and the corresponding optimal minimizer is

$$z_j^* = \begin{cases} u_j, & |u_j| \geq \theta, \\ 0, & |u_j| < \theta. \end{cases}$$

Note that for  $|u_j| = \theta$ ,  $z_j^*$  can be either  $u_j$  or 0, since both solutions give the minimum cost value of (12). This completes the first proof.

Now, for any  $\mathbf{z}$ , according to the optimal solution  $\mathbf{z}^*$ , observe that

$$\|\mathbf{u} - \mathbf{z}\|_1 + \theta \|\mathbf{z}\|_0 \geq \|\mathbf{u} - \mathbf{z}^*\|_1 + \theta \|\mathbf{z}^*\|_0.$$

Considering  $\|\mathbf{z}\|_0 \leq \|\mathbf{z}^*\|_0$  in Proposition 2.1, we have

$$\|\mathbf{u} - \mathbf{z}\|_1 - \|\mathbf{u} - \mathbf{z}^*\|_1 \geq \theta (\|\mathbf{z}^*\|_0 - \|\mathbf{z}\|_0) \geq 0,$$

and this completes the second proof.



Fig. 5. The XCAT phantom in the ROI used for testing in our 3D experiments ( $420 \times 420 \times 64$ ; the slice used for testing in our 2D experiments corresponds to the central axial slice of this phantom; display window is  $[800, 1200]$  HU).

REFERENCES

- [1] G. H. Chen, J. Tang, and S. Leng, "Prior image constrained compressed sensing (PICCS): a method to accurately reconstruct dynamic ct images from highly undersampled projection data sets," *Med. Phys.*, vol. 35, no. 2, pp. 660–663, Feb. 2008.
- [2] I. Y. Chun and T. Talavage, "Efficient compressed sensing statistical X-ray/CT reconstruction from fewer measurements," in *Proc. 12<sup>th</sup> Intl. Mtg. on Fully 3D Image Recon. in Rad. and Nuc. Med.*, Lake Tahoe, CA, Jun. 2013, pp. 30–33.
- [3] S. Foucart and H. Rauhut, *A mathematical introduction to compressive sensing*. New York, NY: Springer, 2013.
- [4] B. Adcock, A. C. Hansen, and B. Roman, "The quest for optimal sampling: Computationally efficient, structure-exploiting measurements for compressed sensing," in *Compressed Sensing and its Applications*, ser. Applied and Numerical Harmonic Analysis, H. B. et al., Ed. Springer, 2015, pp. 143–167.
- [5] I. Y. Chun and B. Adcock, "Compressed sensing and parallel acquisition," *IEEE Trans. Inf. Theory*, vol. 63, no. 7, pp. 1–23, May 2017. [Online]. Available: <http://arxiv.org/abs/1601.06214>
- [6] E. Y. Sidky, C.-M. Kao, and X. Pan, "Accurate image reconstruction from few-views and limited-angle data in divergent-beam CT," *J. X-ray Sci. Technol.*, vol. 14, no. 2, pp. 119–139, 2006.
- [7] H. Yu and G. Wang, "Compressed sensing based interior tomography," *Phys. Med. Biol.*, vol. 54, no. 9, pp. 2791–2805, May 2009.
- [8] J. Bian, J. H. Siewerdsen, X. Han, E. Y. Sidky, J. L. Prince, C. A. Pelizzari, and X. Pan, "Evaluation of sparse-view reconstruction from flat-panel-detector cone-beam CT," *Phys. Med. Biol.*, vol. 55, no. 22, p. 6575, Oct. 2010.
- [9] S. Ramani and J. A. Fessler, "A splitting-based iterative algorithm for accelerated statistical X-ray CT reconstruction," *IEEE Trans. Med. Imag.*, vol. 31, no. 3, pp. 677–688, Mar. 2012.
- [10] S. Niu, Y. Gao, Z. Bian, J. Huang, W. Chen, G. Yu, Z. Liang, and J. Ma, "Sparse-view X-ray CT reconstruction via total generalized variation regularization," *Phys. Med. Biol.*, vol. 59, no. 12, p. 2997, May 2014.
- [11] M. Aharon, M. Elad, and A. Bruckstein, "K-SVD: An algorithm for designing overcomplete dictionaries for sparse representation," *IEEE Trans. Signal Process.*, vol. 54, no. 11, pp. 4311–4322, Nov. 2006.
- [12] J.-F. Cai, H. Ji, Z. Shen, and G.-B. Ye, "Data-driven tight frame construction and image denoising," *Appl. Comput. Harmon. A.*, vol. 37, no. 1, pp. 89–105, Oct. 2014.
- [13] S. Ravishanker and Y. Bresler, " $\ell_0$  sparsifying transform learning with efficient optimal updates and convergence guarantees," *IEEE Trans. Signal Process.*, vol. 63, no. 9, pp. 2389–2404, May 2015.
- [14] I. Y. Chun and J. Fessler, "Convolutional dictionary learning: Acceleration and convergence," *IEEE Trans. Image Process.*, vol. PP, no. 99, p. 0, Oct. 2017.
- [15] I. Y. Chun and J. A. Fessler, "Convergent convolutional dictionary learning using adaptive contrast enhancement (CDL-ACE): Application of cdl to image denoising," in *Proc. 12<sup>th</sup> Sampling Theory and Appl. (SampTA)*, Tallinn, Estonia, Jul. 2017, pp. 460–464.
- [16] Q. Xu, H. Yu, X. Mou, L. Zhang, J. Hsieh, and G. Wang, "Low-dose X-ray CT reconstruction via dictionary learning," *IEEE Trans. Med. Imag.*, vol. 31, no. 9, pp. 1682–1697, Sep. 2012.

- [17] C. Zhang, T. Zhang, M. Li, C. Peng, Z. Liu, and J. Zheng, "Low-dose CT reconstruction via L1 dictionary learning regularization using iteratively reweighted least-squares," *Biomed. Eng. OnLine*, vol. 15, no. 1, p. 66, Jun. 2016.
- [18] X. Zheng, Z. Lu, S. Ravishankar, Y. Long, and J. A. Fessler, "Low dose CT image reconstruction with learned sparsifying transform," in *Proc. 2016 IEEE IVMSPP*, Bordeaux, France, Jul. 2016, pp. 1–5.
- [19] X. Zheng, S. Ravishankar, Y. Long, and J. A. Fessler, "PWLS-ULTRA: An efficient clustering and learning-based approach for low-dose 3D CT image reconstruction," *arXiv preprint stat.ML/1703.09165*, Mar. 2017.
- [20] H. Chen, Y. Zhang, M. K. Kalra, F. Lin, P. Liao, J. Zhou, and G. Wang, "Low-dose ct with a residual encoder-decoder convolutional neural network (RED-CNN)," *IEEE Trans. Med. Imag.*, vol. PP, no. 99, p. 0, Jun. 2017.
- [21] E. Kang, J. Min, and J. C. Ye, "A deep convolutional neural network using directional wavelets for low-dose X-ray CT reconstruction," *Med. Phys.*, vol. 44, no. 10, pp. e360–e375, Oct. 2017.
- [22] J. M. Wolterink, T. Leiner, M. A. Viergever, and I. Isgum, "Generative adversarial networks for noise reduction in low-dose CT," *IEEE Trans. Med. Imag.*, vol. PP, no. 99, p. 0, May 2017.
- [23] K. H. Jin, M. T. McCann, E. Froustey, and M. Unser, "Deep convolutional neural network for inverse problems in imaging," *IEEE Trans. Image Process.*, vol. 26, no. 9, pp. 4509–4522, Sep. 2017.
- [24] H. Chen, Y. Zhang, W. Zhang, H. Sun, P. Liao, K. He, J. Zhou, and G. Wang, "Learned experts' assessment-based reconstruction network ("learn") for sparse-data ct," *arXiv preprint physics.med-ph/1707.09636*, 2017.
- [25] D. Wu, K. Kim, G. E. Fakhri, and Q. Li, "Iterative low-dose CT reconstruction with priors trained by neural network," in *Proc. 14<sup>th</sup> Intl. Mtg. on Fully 3D Image Recon. in Rad. and Nuc. Med.*, Xi'an, China, Jun. 2017, pp. 195–198.
- [26] S. Boyd, N. Parikh, E. Chu, B. Peleato, and J. Eckstein, "Distributed optimization and statistical learning via the alternating direction method of multipliers," *Found. & Trends in Machine Learning*, vol. 3, no. 1, pp. 1–122, Jan. 2011.
- [27] J. B. Thibault, C. A. Bouman, K. D. Sauer, and J. Hsieh, "A recursive filter for noise reduction in statistical iterative tomographic imaging," in *Proc. SPIE 6065, Computational Imaging IV*, vol. 6065, Feb. 2006, p. 60650X.
- [28] I. Y. Chun, B. Adcock, and T. M. Talavage, "Efficient compressed sensing SENSE pMRI reconstruction with joint sparsity promotion," *IEEE Trans. Med. Imag.*, vol. 35, no. 1, pp. 354–368, Jan. 2016.
- [29] S. Ravishankar and Y. Bresler, "Efficient blind compressed sensing using sparsifying transforms with convergence guarantees and application to magnetic resonance imaging," *SIAM J. Imaging Sci.*, vol. 8, no. 4, pp. 2519–2557, Nov. 2015.
- [30] J. A. Fessler and S. D. Booth, "Conjugate-gradient preconditioning methods for shift-variant PET image reconstruction," *IEEE Trans. Image Process.*, vol. 8, no. 5, pp. 688–699, May 1999.
- [31] S. D. Booth and J. A. Fessler, "Combined diagonal/Fourier preconditioning methods for image reconstruction in emission tomography," in *Proc. 1995 ICIP*, vol. 2, Washington, DC, Oct. 1995, pp. 441–444.
- [32] L. Fu, Z. Yu, J.-B. Thibault, B. De Man, M. McGaffin G., and J. A. Fessler, "Space-variant channelized preconditioner design for 3D iterative CT reconstruction," in *Proc. 12<sup>th</sup> Intl. Mtg. on Fully 3D Image Recon. in Rad. and Nuc. Med.*, Lake Tahoe, CA, Jun. 2013, pp. 205–208.
- [33] L. Fu, J. A. Fessler, P. E. Kinahan, and B. De Man, "Combining non-diagonal preconditioning and ordered-subsets for iterative ct reconstruction," in *Proc. 14<sup>th</sup> Intl. Mtg. on Fully 3D Image Recon. in Rad. and Nuc. Med.*, Xi'an, China, Jun. 2017, pp. 760–766.
- [34] W. P. Segars, M. Mahesh, T. J. Beck, E. C. Frey, and B. M. W. Tsui, "Realistic CT simulation using the 4D XCAT phantom," *Med. Phys.*, vol. 35, no. 8, pp. 3800–3808, Jul. 2008.
- [35] L. A. Feldkamp, L. C. Davis, and J. W. Kress, "Practical cone beam algorithm," *J. Opt. Soc. Am. A*, vol. 1, no. 6, pp. 612–9, Jun. 1984.
- [36] J. H. Cho and J. A. Fessler, "Regularization designs for uniform spatial resolution and noise properties in statistical image reconstruction for 3-D X-ray CT," *IEEE Trans. Med. Imag.*, vol. 2, no. 34, pp. 678–689, Feb. 2015.
- [37] H. Nien and J. A. Fessler, "Relaxed linearized algorithms for faster X-ray CT image reconstruction," *IEEE Trans. Med. Imag.*, vol. 35, no. 4, pp. 1090–1098, Apr. 2016.
- [38] J. A. Fessler and W. L. Rogers, "Spatial resolution properties of penalized-likelihood image reconstruction methods: Space-invariant tomographs," *IEEE Trans. Image Process.*, vol. 5, no. 9, pp. 1346–58, Sep. 1996.
- [39] I. Y. Chun, X. Zheng, Y. Long, and J. A. Fessler, "Sparse-view X-ray CT reconstruction using  $\ell_1$  regularization with learned sparsifying transform," in *Proc. 14<sup>th</sup> Intl. Mtg. on Fully 3D Image Recon. in Rad. and Nuc. Med.*, Xi'an, China, Jun. 2017, pp. 115–119.